

Anticipating the *XRISM* search for the decay of resonantly produced sterile neutrino dark matter

Mark R. Lovell¹★

¹*Centre for Astrophysics and Cosmology, Science Institute, University of Iceland, Dunhaga 5, 107 Reykjavík, Iceland*

Accepted XXX. Received YYY; in original form ZZZ

ABSTRACT

The resonantly produced sterile neutrino (N_1) of the neutrino minimal standard model (ν MSM) is a compelling dark matter candidate, especially in the reported possible detection of N_1 with mass $m_s = 7.1$ keV in X-ray decay. This particle will be accessible to the *XRISM* X-ray mission over the next 12 months. We revisit the physics behind N_1 and the uncertainty in its parameters. We compare predictions for the $m_s = 7.1$ keV N_1 mixing angle, $\sin^2(2\theta)$, and half-mode mass, M_{hm} , to existing X-ray observations and structure formation constraints. The strongest available constraints rule out N_1 as a dark matter candidate, and a more optimistic reading of the data prefers $\sin^2(2\theta) = 5 \times 10^{-11}$ and $M_{\text{hm}} = 3.5 \times 10^8 M_\odot$. We highlight that the most promising upcoming opportunity for a detection is to find a line of velocity dispersion $\sim 500 \text{ km s}^{-1}$ in the Virgo cluster with *XRISM*, and then draw up a list of future objects of study to determine: (i) whether the line is from dark matter generally, and (ii) if from dark matter, whether that candidate is indeed N_1 .

Key words: dark matter – neutrinos – early Universe

1 INTRODUCTION

The nature of dark matter remains one of the most important outstanding puzzles in astrophysics, cosmology, and particle physics. Constraints on candidate dark matter particles come in two forms: (i) astrophysical-cosmological, which constitute the impact that a dark matter particle has on its environment, and (ii) particle constraints, which are laboratory experiments – including collider generation and relic dark matter scattering off standard model particles – and attempts to detect radiation from dark matter that decays or annihilates. The second set of constraints is a necessary condition for any claim to have identified the dark matter, and the first set is an important extra condition that applies to the subclass of models for which dark matter has self-interactions or a cutoff at mass scales $> 10^7 M_\odot$.

One such model of interest is the resonantly produced sterile neutrino (Shi & Fuller 1999; Laine & Shaposhnikov 2008). This particle has a mass at the keV scale, and constitutes part of a broader standard model extension that also has the potential to explain baryogenesis and neutrino oscillations (Asaka & Shaposhnikov 2005; Boyarsky et al. 2009a). It undergoes free-streaming to a degree that affects the number of dwarf galaxies (Bode et al. 2001; Lovell et al. 2014) and generates an X-ray decay signal (Pal & Wolfenstein 1982), thus it is subject to both the astrophysical constraints and the particle constraints discussed above. A candidate X-ray decay signal from a putative 7.1 keV-mass particle has been reported in galaxy clusters, the M31 galaxy and in the halo of the Milky Way (MW) (e.g. Boyarsky et al. 2014; Bulbul et al. 2014; Cappelluti et al. 2018; Hofmann & Wegg 2019). The interpretation of these results as dark matter decay is controversial (e.g. Anderson et al. 2015; Jeltema & Profumo 2016; Dessert et al. 2020b). Further light is ex-

pected to be shed on this subject by the launch of the JAXA *XRISM* mission in May 2023 (Terada et al. 2021), where a detection of the line, and subsequently a measurement of the lines' velocity dispersion, would constitute a particularly compelling piece of evidence for a dark matter decay origin (Lovell et al. 2019b).

If a detection of this line were made, the next step would be to determine whether this general dark matter decay signal corresponds specifically to a resonantly produced sterile neutrino or instead to a still more exotic dark matter candidate. This analysis constitutes computing the expected particle physics parameters consistent with the notional *XRISM* detection – sterile neutrino mass and mixing angle – and comparing these results to constraints from X-ray non-detections and from structure formation constraints. The resonantly produced sterile neutrino model consistent with the reported X-ray detections is especially suitable for this analysis, because relaxing X-ray constraints requires a smaller mixing angle, which in turn generates a large-scale cutoff in the linear matter power spectrum and thus stronger structure formation constraints (Lovell et al. 2016).

In this paper we revisit the physics of resonantly produced sterile neutrino dark matter in the cosmological context. We discuss the relationship between the sterile neutrino parameters on the one hand and its decay/free-streaming properties on the other, while illustrating in particular the systematic uncertainty in the calculation of the free-streaming scale. We compare the decay rate and free-streaming results to existing X-ray and structure formation constraints. We highlight the putative sterile neutrino parameters that we might expect for a line detected by *XRISM*, and end by outlining the following steps required to determine whether resonantly produced sterile neutrinos are indeed the dark matter.

This paper is organised as follows. In Section 2 we discuss the physics of sterile neutrinos as dark matter, and in Section 3 we compute matter power spectra and present the possible model physics

★ E-mail: lovell@hi.is

parameters. We compare the results to observations in Section 4 and draw conclusions in Section 5.

2 RESONANTLY PRODUCED STERILE NEUTRINO DARK MATTER

2.1 Introducing three extra neutrinos

The original motivation for sterile neutrinos comes from observations of two unexplained phenomena in neutrino physics: the absence of right-handed neutrinos and neutrino oscillations. First, neutrinos are the only standard model fermion that have only ever been observed to have left-handed chirality, therefore it is reasonable to posit the existence a counterpart right-handed chirality neutrino to match the rest of the standard model. This particle is known as a ‘sterile’ neutrino because its right-handed chirality suppresses its coupling to the weak force, as compared to the left-handed ‘active’ neutrino of the standard model. Such a neutrino would then be expected to explain the observation of neutrino flavour oscillations. These oscillations can only occur if the neutrinos have mass, whereas the standard model of particle physics assumes that neutrinos are strictly massless. Sterile neutrinos may then endow standard model neutrinos with mass through processes such as the seesaw mechanism. Under this condition the masses of the sterile neutrinos are unconstrained, and models have been proposed in which the mass could be as large as a TeV (Humbert et al. 2015) or as small as an eV, the latter of which is known as a ‘light sterile neutrino’ and has been proposed to explain several neutrino experiment anomalies (Athanasopoulos et al. 1996; Mention et al. 2011).

One specific model of note is the neutrino minimal standard model, the ν MSM, which adds exactly three sterile neutrinos to the standard model (Asaka & Shaposhnikov 2005; Boyarsky et al. 2009a). Under this model, two of the sterile neutrinos are responsible for facilitating neutrino oscillations. These two particles have short lifetimes and are almost degenerate in mass, and are much more massive than the third sterile neutrino, in a manner that reflects the mass differences of the active neutrino mass eigenstates.

This model is especially compelling when the model parameters are set such that they can explain two additional outstanding problems in particle physics: baryogenesis and dark matter. Baryogenesis is achieved through low-scale leptogenesis, in which the two more massive sterile neutrinos preferentially decay into anti-leptons that are subsequently converted into baryons via the weak interaction sphaleron process, and thus leads to the required excess of baryons over anti-baryons. Moreover, the ability to generate an imbalance between leptons and anti-leptons – known as the lepton asymmetry – enhances the likelihood of active neutrinos oscillating into the lower mass sterile neutrino in a manner similar to the Mikheyev–Smirnov–Wolfenstein effect (Wolfenstein 1978; Mikheev & Smirnov 1986) that alters the oscillation rates of active neutrinos; this process is known as *resonant-production* (Shi & Fuller 1999; Dolgov & Hansen 2002).

This sterile neutrino has a lifetime much longer than the age of the Universe, and via the oscillation method can be generated in sufficient quantities to match the measured dark matter abundance. It also decouples immediately from the primordial plasma on production – a process known as freeze-in – and therefore evades bounds from Big Bang nucleosynthesis (BBN) and the cosmic microwave background (CMB) that otherwise constrain light dark matter particles (Sabti et al. 2020; An et al. 2022). Finally, these three phenomena – neutrino oscillations, baryogenesis, and dark matter – can be explained simultaneously if the masses of the two more massive sterile

neutrinos fall in the \sim GeV regime and the lower mass sterile neutrino is a million times less massive, and thus in the \sim keV regime. Throughout the rest of this paper we will refer to the GeV-scale heavier sterile neutrinos in this specific model as N_2 and N_3 , and to the keV-scale sterile neutrino as N_1 .

2.2 Production of sterile neutrino dark matter

The effect of the lepton asymmetry on the production has an important impact on the permitted sterile neutrino parameters. In the absence of a lepton asymmetry, the production rate is set by the particle mass and the mixing angle from sterile to active neutrinos, $\sin^2(2\theta)$ (Dodelson & Widrow 1994). The resonance effect promotes the conversion of lower energy active neutrinos to sterile neutrinos, thus lowering the velocity dispersion of the sterile neutrinos compared to what would be expected if the resonance were absent. This lepton asymmetry can be parametrized in multiple different ways, such as the difference in lepton and anti-lepton densities prior to dark matter production divided by the entropy density, or instead divided by the photon density. In this paper we adopt the entropy density normalisation L_6 , which is defined as:

$$L_6 = 10^6 \left(\frac{n - \bar{n}}{s} \right), \quad (1)$$

where n is the lepton density, \bar{n} is the anti-lepton density, and s is the entropy density. Results normalized in other studies by the photon density – sometimes referred to as L_4 – can be converted into L_6 equivalents through multiplying by 5.4×10^{-3} ; we refer the reader to the appendix of Laine & Shaposhnikov (2008) for a comprehensive discussion.

The relationship of \sim keV mass N_1 to the standard model provides a very different detection paradigm to that of other dark matter candidates. Constraints on the parameters of potential supersymmetric weakly interacting massive particles (WIMPs) are set by non-detections at large annihilation interaction rates, and also depend on the complicated interactions that lead from the original annihilation to detectable products; lower bounds on the interaction are set from theoretical considerations (see Gaskins 2016, for a review). N_1 differ in that, for the range of $\sin^2(2\theta)$ of interest, the ‘interaction rate’ – in this case the mixing angle between sterile neutrinos and standard model neutrinos – correlates inversely with the mean velocity dispersion. The increase in velocity dispersion erases structures on progressively larger mass scales through free-streaming, and thus inhibits the formation of dwarf galaxies to a degree that is accessible to structure formation measurements. Therefore, the N_1 mixing angle is bounded by X-ray decay constraints from above and structure formation constraints from below.

The dominant decay channel of a sterile neutrino is to three active neutrinos (Barger et al. 1995), and the subdominant X-ray decay channel is a two-body decay into an X-ray photon and a neutrino. In the latter case, conservation of momentum and energy determine that the photon energy will always be half the rest mass of the parent sterile neutrino, m_s , thus the mass will always be twice the rest-frame energy centroid of any measured line. The relationship between $\sin^2(2\theta)$ and measured X-ray flux is relatively straightforward, and follows the relation:

$$\Gamma_\gamma = 1.38 \times 10^{-29} \text{s}^{-1} \left(\frac{\sin^2(2\theta)}{10^{-7}} \right) \left(\frac{m_s}{\text{keV}} \right)^5, \quad (2)$$

as discussed in Pal & Wolfenstein (1982); Barger et al. (1995);

Boyarsky et al. (2014); Bulbul et al. (2014); $\Gamma_\gamma \approx \Gamma_{\nu\nu\nu}/128$ where $\Gamma_{\nu\nu\nu}$ is the decay rate in the dominant three-neutrino channel. $\sin^2(2\theta)$ is also related to the production rate of dark matter in the early Universe. The maximum possible value of $\sin^2(2\theta)$ at a given mass is set by the measured dark matter abundance, and this defines non-resonant production. The presence of a lepton asymmetry enhances the production rate as discussed above, which then requires a lower $\sin^2(2\theta)$. At a sufficiently low value of $\sin^2(2\theta)$ no value of L_6 is able to generate enough sterile neutrinos to match the measured dark matter abundance and thus one obtains a hard lower limit on $\sin^2(2\theta)$.

In addition to the overall abundance of sterile neutrinos, the combination of mass, mixing angle, and lepton asymmetry also sets the sterile neutrino momentum distribution, and by extension the free-streaming scale, as mentioned above. A comprehensive discussion is presented in Lovell et al. (2016), here we provide a brief summary. Increasing L_6 promotes the resonant production of sterile neutrinos below some momentum threshold, and this momentum threshold itself increases with L_6 . Therefore, decreasing $\sin^2(2\theta)$ from its maximum value – the non-resonant production value – leads to a colder momentum distribution up to some characteristic value, beyond which the resonance momentum threshold is sufficiently high that the momentum distribution becomes warmer once again until eventually it is identical to the initial, non-resonant distribution. For the $m_s = 7.1$ keV sterile neutrino the distribution is maximally cold at $\sin^2(2\theta) \sim 2 \times 10^{-10}$, which is also the upper limit on $\sin^2(2\theta)$ expected from the reported M31 3.55 keV line detection when the maximum uncertainty on the M31 mass is applied (Boyarsky et al. 2014).

The momentum distribution can then be supplied to a Boltzmann solver code, such as CAMB (Lewis et al. 2000) or CLASS (Lesgourgues & Tram 2011) to obtain a matter power spectrum, which in turn can be fed into cosmological simulations and semi-analytic models to estimate structure formation constraints. These constraints are typically described with parameters that apply to dark matter models beyond sterile neutrinos, such as the mass scale at which the square root of the ratio of dark matter power spectrum relative to that of cold dark matter (CDM) is 50 per cent: this is known as the half-mode mass, M_{hm} . Another choice is the thermal relic mass m_{th} , which is the mass of a notional thermal relic particle with a matter power spectrum that in some way approximates the dark matter model in question. In summary, X-ray detections and non-detections inform the permitted values of m_s and $\sin^2(2\theta)$, and subsequent work is required to estimate the value of L_6 and also M_{hm} for the purpose of obtaining astrophysics/cosmology constraints.

In practice, the ability to compute the lepton asymmetry and momentum distribution from the dark matter abundance, m_s and $\sin^2(2\theta)$ is non-trivial. Tracking the generation of sterile neutrinos from energies as high as 100 GeV through to 10 MeV – where production ceases – involves computing the distribution of energies across the boundary where the quark–gluon plasma condenses into bound baryons, at around 150 MeV (Petreczky 2012), and also requires the computation of short-lived resonances in the lepton sector. Ghiglieri & Laine (2015) (hereafter GL15) and Venumadhav et al. (2016) (VE16) released public codes with the goal of computing these quantities, and demonstrated that differences in the modelling of neutrino interactions can have a large impact on the required L_6 at mixed $\sin^2(2\theta)$ and m_s – GL15 alone showed differences of a factor of 10 in the six cases it considered – and that they will also have an impact on the matter power spectrum.

2.3 Summary of timescales and additional sterile neutrino models

We summarise some of the key points above by computing rough estimates of the temperatures and timescales, and present these in Fig. 1. We indicate the scale at which sphaleron processes come to an end – $T \sim 10^5$ MeV and $t \sim 10^{-10}$ sec – which also marks the closure of low-scale baryogenesis in the ν MSM; the approximate quark–hadron transition at just above 10^2 MeV and the start of BBN at 0.8 MeV. We then show the production time of N_1 as computed from VE16, which occurs between 10^{-5} and 10^{-2} sec after the Big Bang, and also the approximate time at which N_1 become non-relativistic, we calculate to be ~ 9 yr after the Big Bang for $\sin^2(2\theta) = 2 \times 10^{-11}$ and a slightly shorter period for cooler models.

This time of 9 yr is well before matter–radiation equality, which is $\gtrsim 50\,000$ yr after the Big Bang. Therefore, it is the case that the N_1 are relativistic during BBN. In principle, dark matter that is relativistic during BBN leads to a faster expansion rate and the injection of energy through annihilations, with the consequence that the helium fraction is drastically altered. Such considerations have ruled out thermal relic particles at the keV scale (Depta et al. 2019; Sabti et al. 2020), but N_1 are completely inert and have no influence on the baryons at this epoch, and therefore evade these bounds. We have also performed a first order calculation of the change to the time period over which neutron decay is possible and thus the helium fraction is set: we find that the density parameter of N_1 at this time is $\Omega_{N_1} \sim 7 \times 10^{-7}$, and the time period of neutron decay is the same as non-relativistic dark matter to less than one part in a million. We assume for the purposes of this study that N_1 does not interfere with BBN, and defer a more careful study to future work.

The most obvious challenge for this model to overcome is the opportunity for X-ray decay and structure formation constraints, which we discuss in Section 4. An alternative method of ruling out this model is to instead make a positive detection of sterile neutrinos that have different parameters to those of the ν MSM. The most prominent example is the light sterile neutrino, which is proposed to have a mass at the eV scale and to explain anomalies measured in the LSND and MiniBOONE experiments (Athanasopoulos et al. 1996; Mention et al. 2011) but would not be a dark matter candidate. Recent analyses by the OPERA and MicroBOONE experiments have determined that these anomalies are in fact not present in their data (Agafonova et al. 2022; Abratenko et al. 2023). Therefore, the likelihood of the existence of the light sterile neutrino is diminished and thus this challenge to the ν MSM version of sterile neutrino physics is no longer as salient. Further alternatives include sterile neutrinos generated from heavy scalars (Merle et al. 2016), TeV scale particles (Humbert et al. 2015) and production from light mediators of active neutrino interactions (An et al. 2023). In the case of decay detection, some of these options may produce the same result as the ν MSM, in which case structure formation constraints will take on extra importance.

In conclusion: we have discussed the background and merits of N_1 as a dark matter candidate, and outlined the challenges faced in estimating model parameters. In Section 3 we will apply the GL15 and VE16 codes to compute distribution functions and matter power spectra, illustrate the differences in these parameters between computational approaches, and compare the results to current constraints.

3 COMPUTATION OF MODEL PARAMETERS

We begin our analysis with the computation of a series of N_1 momentum distributions and their corresponding matter power spectra. We

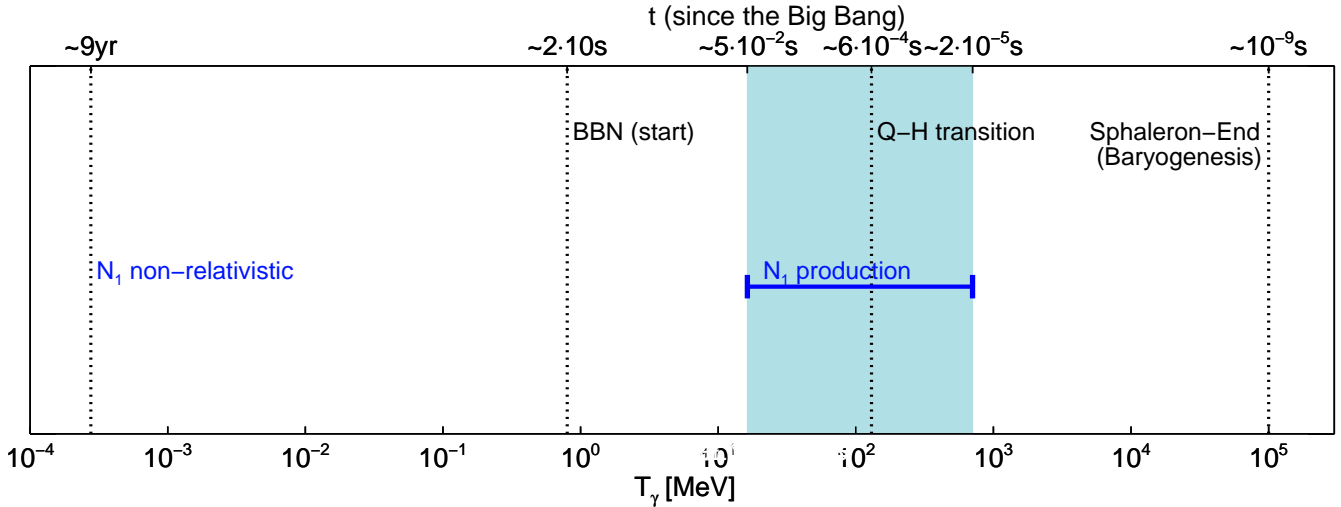


Figure 1. Rough illustration of energy scales associated with the production of N_1 , where the energy scales are denoted with the photon temperature T_γ . The labelled energy scales are the start of BBN, the quark-hadron transition, the end of the sphaleron process, the epoch of N_1 production and the energy at which N_1 become non-relativistic. Approximate timescales are indicated on the upper x -axis.

illustrate the differences between the predictions of different models, compare their results to the thermal relic model expectations and compute some key parameter values.

3.1 Linear matter power spectra

Our momentum distributions are computed as follows. We assume $m_s = 7.1$ keV, as inspired by the 3.55 keV line, and adopt ten values of $\sin^2(2\theta)$ in the range $[2, 20] \times 10^{-11}$ to span the broadest range of viable $\sin^2(2\theta)$ inferred from the 3.55 keV line detection of Boyarsky et al. (2014) in M31. We then compute momentum distributions for these ten mixing angles using the publicly available codes of VE16 and GL15. The latter code includes six different cases, labelled a-f: for all of the computations in this paper we adopt their case (d) mode as this the default non-equilibrium calculation presented in their online distribution. Also, this code determines cosmological abundance as a function of L_6 rather than the other way round, therefore we iterate over L_6 values to obtain an abundance that is within 1 per cent of the measured cosmological dark matter abundance. We then compute matter power spectra using Boltzmann codes: CLASS (Lesgourgues & Tram 2011) and a modified version of CAMB (Lewis et al. 2000; Boyarsky et al. 2009b), using the cosmological parameters determined in (Planck Collaboration et al. 2016). This gives us four combinations of codes; we first plot the results for VE16 processed with CLASS and GL15 processed with CAMB in Fig. 2, as this turns out to be the most divergent set of code combination power spectra.

Both codes return the familiar pattern in which the matter power spectrum exhibits a cutoff, and the wavenumber of the cutoff increases with $\sin^2(2\theta)$ ¹. Where the two codes differ is in their predictions for the power spectrum shape: the GL15 results turnover slope is shallower than for VE16. This behaviour is more clearly apparent in the ratio with respect to CDM as shown in the bottom panel

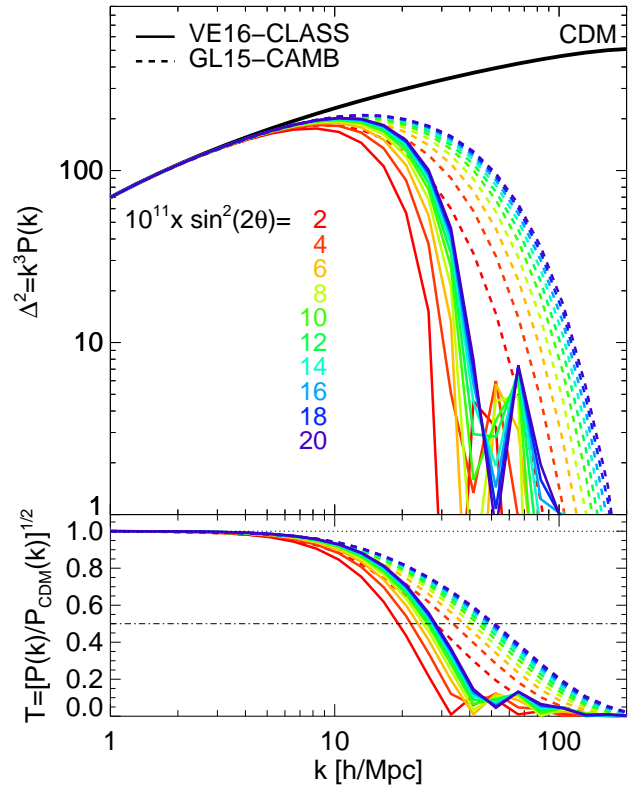


Figure 2. The dimensionless matter power spectra for dark matter models. N_1 power spectra mixing angles are indicated by their colour in the figure legend. VE16 spectra are indicated with solid lines and GL15 with dashed lines. In the top panel CDM is indicated with a solid black panel; in the bottom panel we plot the transfer function of the N_1 power spectra with respect to CDM.

¹ Still larger values of $\sin^2(2\theta)$ would exhibit a turnaround in behaviour, where the cutoff shifts back to smaller wavenumbers as discussed in the previous section. However, these are outside the expected 3.55 keV line constraints and therefore are not considered here.

of Figure 2. It is also apparent from this panel that the half mode wavenumber is marginally larger for GL15 than it is for VE16, thus the value of M_{hm} will be smaller for the former. Finally, we note that the VE16 generates sharp peaks at scales much smaller than the cut-

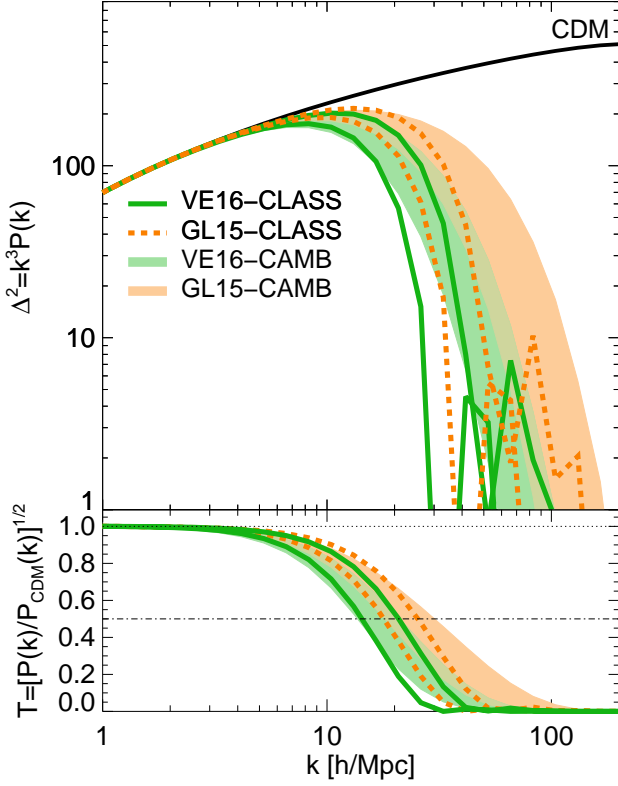


Figure 3. The dimensionless matter power spectra for different combinations of momentum codes and Boltzmann codes. In all four cases the delineated region is bounded by the curves for $\sin^2(2\theta) = 2 \times 10^{-11}$ at the low- k end and $\sin^2(2\theta) = 2 \times 10^{-10}$ at the high- k end. The brown (green) shaded regions mark the data range obtained for the GL15 (VE16) codes with the CAMB, and the dashed brown and solid green lines show the same for the case when CLASS is used. The CDM power spectrum is shown with a solid black line. In the bottom panel we indicate the transfer functions for the four code combinations.

off scale; we anticipate that these may be due to numerical noise, and they are unlikely to be relevant for structure formation constraints.

In the previous figure, we indicated the maximum difference in potential matter power spectra between different implementations of the relevant codes. We break this down further by computing the allowed region of parameter spectra for all four combinations of codes – VE16-CLASS, VE16-CAMB, GL15-CLASS, GL15-CAMB – and plot these together in Fig. 3. Note that the CLASS versions were run with the default resolution rather than with the high resolution option, because the high resolution implementation was unable to obtain a fit to the momentum distributions.

For both momentum codes CAMB generates a shallower cutoff than does CLASS. The former starts to turnover at slightly lower wavenumbers than the latter, thus the amplitude of the CLASS curves is a few per cent higher than in CAMB. The CLASS curves then drop dramatically, leaving much more power in CAMB at small scales. This leaves significant differences in the half mode wavenumber, especially for the cooler GL15 models where the two Boltzmann codes differ at the tens of per cent scale. We conclude that the choice of Boltzmann solver is a source of uncertainty in the calculation of the power spectra, although much smaller than the uncertainty due to the choice of momentum code.

The existence of a cutoff at scales corresponding to dwarf galaxies means that N_1 are classed as warm dark matter (Bond & Szalay

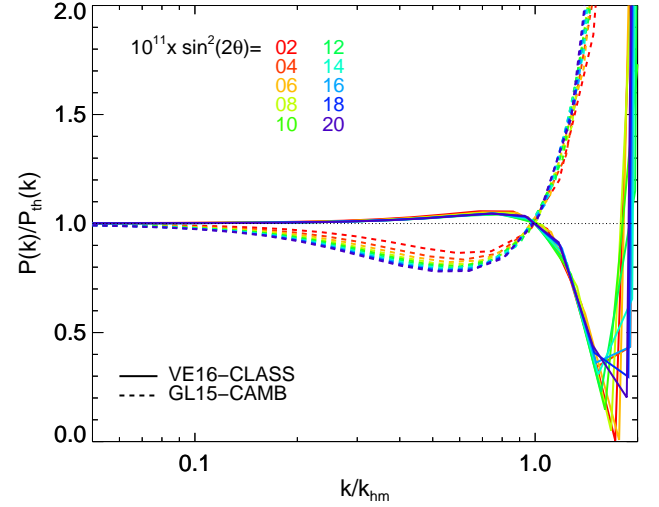


Figure 4. The ratio of the N_1 matter power spectra with respect to the Viel et al. (2005) thermal relic approximation that has the same half-mode mass / half-mode wavenumber. Mixing angles are indicated by their colour in the figure legend. VE16 spectra calculated with CLASS are indicated with solid lines and GL15 calculated with CAMB as dashed lines.

1983; Bardeen et al. 1986; Bode et al. 2001). Given the desire to have constraints on dark matter cutoffs that are not dependent on any single particle physics candidate, it is common to generate constraints for the thermal relic toy model discussed above. In practice, this is typically achieved through the fit to thermal relic spectra computed in Viel et al. (2005), which links the thermal relic mass m_{th} to M_{hm} as outlined in Bose et al. (2016a). The Viel et al. (2005) relation in principle does not need to have the same shape as the N_1 spectra. Therefore, for each of our N_1 curves we compute the half-mode mass M_{hm} and then in turn compute the Viel et al. (2005) power spectrum that has the same M_{hm} . We compute the ratio of each N_1 power spectrum to its same- M_{hm} thermal relic counterpart and present the results in Fig. 4. We divide the wavenumber by each models’ have-mode wavenumber, therefore the value of the ratio at k/k_{hm} equals 1 by construction. Finally, we showed in Fig. 3 that the choice of Boltzmann solver has an impact on the shape, we therefore show the VE16-CLASS and Ghiglieri & Laine (2015)-CAMB results, and comment on the differences with the other two code combinations in the text.

The VE16-CLASS calculations track the thermal relic approximation very closely for $k < k_{\text{hm}}$, the latter underestimates the former by less than 10 per cent at $k \sim 0.6k_{\text{hm}}$, then drops rapidly at smaller scales before experiencing a likely unphysical rise close to $k \sim 2k_{\text{hm}}$. This behaviour is of the same magnitude for all values of $\sin^2(2\theta)$, and the GL15-CLASS versions are identical. The shallower cutoff of GL15-CAMB provides very different behavior, with up to 20 per cent less power in the N_1 curve than in its thermal relic approximation, before rapidly rising in relative power at scales smaller than k_{hm} . Also, the difference between N_1 and the approximation is strongly dependent on $\sin^2(2\theta)$, with stronger deviations for larger values of $\sin^2(2\theta)$. The VE16-CAMB results (not shown) also predict less power in the N_1 curves than in the thermal relic approximation, but to a lesser extent than for GL15-CAMB: 10 per cent for $\sin^2(2\theta) = 2 \times 10^{-10}$ and smaller suppressions for lower $\sin^2(2\theta)$ values. We therefore expect that the Viel et al. (2005) thermal relic is an excellent approximation to the CLASS results computation but may slightly overestimate the power in CAMB, especially for the GL15 momentum computations.

3.2 Parameter values: lepton asymmetry and the half-mode mass

We have demonstrated that the momentum distribution computation algorithm, Boltzmann solver and parameter choices have a significant impact on the shape and position of the cutoff for fixed $\sin^2(2\theta)$ and m_s , and will therefore have an impact on M_{hm} . We also stated in Section 2 that the value of L_6 required to obtain the correct abundance will also differ substantially. We illustrate the scale of these differences explicitly by computing L_6 as a function of $\sin^2(2\theta)$ for both codes, and M_{hm} for all four code combinations, and then presenting the results in Fig. 5. We also include the results of previously unpublished computations for the 7.1 keV N_1 using the machinery behind Lovell et al. (2016) and subsequent papers that build on that paper, which itself used an earlier version of the GL15 code. We include these results to facilitate comparisons to earlier work; understanding the origins of these differences is beyond the scope of this paper.

The values of L_6 differ significantly between the three computational implementations. All three follow the familiar track wherein smaller mixing angles require larger lepton asymmetries to obtain the correct abundance, but the amplitudes of the relations differ considerably. VE16 prefers $L_6 = 18$ at $\sin^2(2\theta) = 2 \times 10^{-11}$ down to $L_6 = 13.5$ at $\sin^2(2\theta) = 2 \times 10^{-10}$, whereas the chosen implementation of GL15 prefers $L_6 = 19$ to $L_6 = 17$ over the same range. We stress that this result applies to one specific implementation of GL15: alternative choices for the initial asymmetries of separate lepton species can generate overall asymmetries at $\sin^2(2\theta) = 2 \times 10^{-11}$ that are as high as $L_6 = 102.77$ or as low as $L_6 = 13.47$, as discussed in GL15 table 1. This lower value is somewhat closer to the Lovell et al. (2016) implementation, which otherwise requires L_6 values much lower than either VE16 or our adopted GL15 implementation. Therefore, there remains work to be done to estimate the initial lepton asymmetry precisely and accurately.

While the value of L_6 is inaccessible to current experiments, M_{hm} is regularly subject to constraints. All four momentum code–Boltzmann code combinations return the familiar anti-correlation between $\sin^2(2\theta)$ and M_{hm} , such that attempts to evade X-ray constraints on $\sin^2(2\theta)$ lead to stronger structure formation constraints on M_{hm} and vice versa. The amplitude of the relations is significantly different, with the smaller scale power spectrum cutoffs of GL15 discussed in 2 leading to smaller M_{hm} by a factor of 2–3 than for VE16 at fixed $\sin^2(2\theta)$ and similarly lower M_{hm} by a factor of 1.5–2 for CAMB than for CLASS, although ultimately it is the momentum code that has the larger impact. The Lovell et al. (2016) implementation generates a somewhat steeper relation, with M_{hm} some 50 per cent larger than GL15 at $\sin^2(2\theta) = 2 \times 10^{-11}$ but approaches the GL15 values towards higher $\sin^2(2\theta)$. Finally, we generate fits to both implementations of the form:

$$M_{\text{hm}} = A \cdot 10^8 M_{\odot} \left(10^{11} \times \sin^2(2\theta)\right)^{-\beta}, \quad (3)$$

where for VE16–CLASS: $A = 9.5$, $\beta = 0.55$; GL15–CLASS: $A = 5.0$, $\beta = 0.57$; VE16–CAMB: $A = 6.8$, $\beta = 0.65$; GL15–CAMB: $A = 2.0$, $\beta = 0.80$.

4 COMPARISON TO OBSERVATIONS

In this section we assess the current status of X-ray detections and constraints on $\sin^2(2\theta)$, and of structure formation constraints on M_{hm} . We then compare some of these constraints to our fits for VE16 and GL15.

4.1 X-ray detections and constraints

The first reported detections of an X-ray line at 3.55 keV consistent with dark matter decay were made by Bulbul et al. (2014) in clusters of galaxies with the *XMM-Newton* (*XMM*) observatory and Boyarsky et al. (2014) in the M31 galaxy and the Perseus galaxy cluster, also with *XMM*. The values of $\sin^2(2\theta)$ were estimated as $6.8^{+1.4}_{-1.4} \times 10^{-11}$ (1σ errors) for the cluster stack and $4.9^{+1.6}_{-1.3} \times 10^{-11}$ for M31 on flux statistical uncertainties alone; including M31 mass uncertainties gives $[2 - 20] \times 10^{-11}$. The detection in the centre of Perseus was anomalously high compared to the other results and subsequently ruled out by Aharonian et al. (2017). Further detections have been reported in the MW Galactic Bulge at $\sim 1^\circ$ from the Galactic Centre with *Chandra* ($2.3 \pm 1.8 \times 10^{-11}$, Hofmann & Wegg 2019) and the MW halo contribution to the COSMOS Legacy and Extended *Chandra* Deep Field South survey fields, also with *Chandra* ($\sim 0.5 - 4 \times 10^{-10}$, Cappelluti et al. 2018). Other studies have reported constraints that are in strong tension with the claimed detections, including in alternative studies of the Galactic Centre (Jeltema & Profumo 2015), the broader MW halo (Dessert et al. 2020b, see also Boyarsky et al. 2020; Dessert et al. 2020a) and still further studies allow for only a small region of the parameter space of interest to remain (Sicilian et al. 2022). A stack of galaxies returned strong constraints (Anderson et al. 2015), which motivated exotic dark matter models in which the line was only generated in clusters (Conlon & Powell 2015). Arguably the most promising target for a detection is the Draco dwarf spheroidal galaxy (Lovell et al. 2015), yet 1.4 Msec observation with XMM-Newton was insufficient to obtain a detection, and two different groups returned different results (Jeltema & Profumo 2016; Ruchayskiy et al. 2016).

Much of the above uncertainty reflects different approaches to modelling the astrophysical background. An alternative source for the line is charge exchange, in which electrons are accreted from the neutral medium onto sulphur atoms and then generate 3.55 keV photons through the subsequent cascade of atomic transitions (Gu et al. 2015; Shah et al. 2016), resulting in an astrophysical line. One key discriminator between a dark matter decay line and an astrophysical line is its velocity dispersion. Astrophysical line velocity dispersions are typically $< 200 \text{ km s}^{-1}$, while Lovell et al. (2019b) showed that for nearby clusters the velocity dispersion is instead 450–800 km s^{-1} depending on the cluster. This measurement requires a high resolution X-ray calorimeter not available to the galaxy cluster studies discussed above. It had been hoped that the *Hitomi* mission would make the required measurement with its state-of-the-art calorimeter, but the mission was lost after a month and the data obtained prior to the failure were not sufficient to detect the line feature (Aharonian et al. 2017). The next opportunity to test the line velocity dispersion will come with the *XRISM* mission (Terada et al. 2021).

4.2 Structure formation and cosmological constraints

Cosmological and structure formation constraints have been derived in a wide variety of astronomical observables, including the CMB, BBN, the Lyman- α forest, gravitational lensing, stellar streams around the MW, reionization studies and MW satellite counts. We summarise the status of each of these fields below. Many of the cosmological constraints are defined for a generic thermal relic WDM model. They typically assume the WDM thermal relic power spectrum using the m_{th} parameter; recall that this reflects an approximation to the N_1 power spectrum and is not the same as the N_1 mass. Throughout this section we will refer to constraints on the WDM model rather than N_1 , except where noted otherwise.

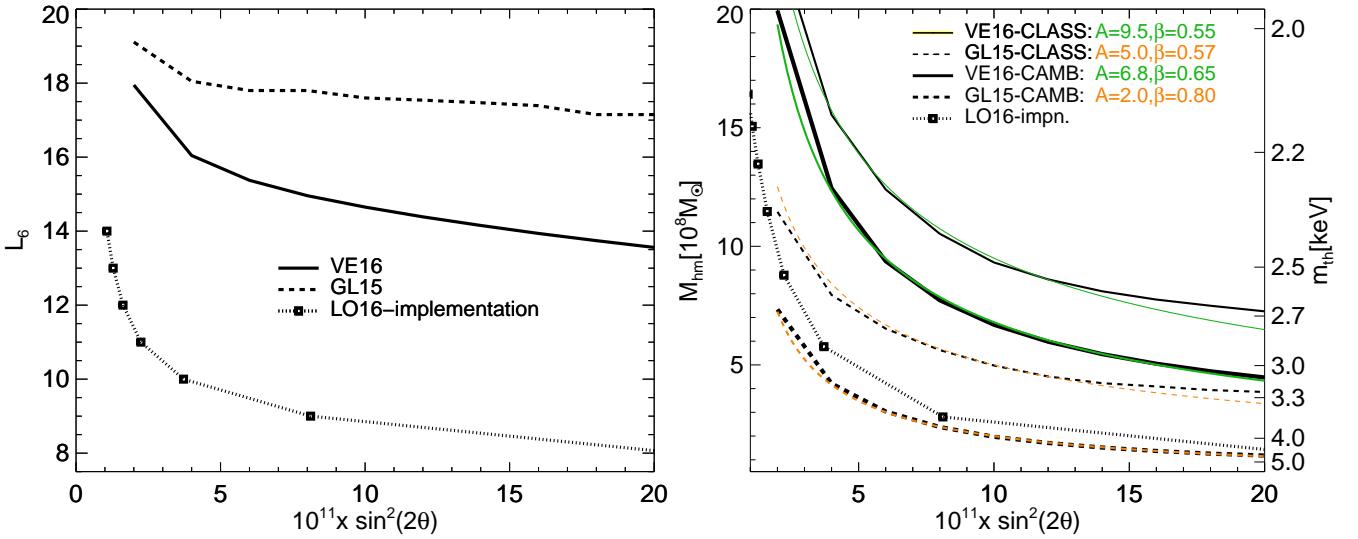


Figure 5. Model properties as a function of the mixing angle for different computational implementations. Left-hand panel: lepton asymmetry L_6 . Right-hand panel: half-mode mass M_{hm} with the corresponding thermal relic particle mass m_{th} indicated on the right-hand y-axis. In both panels **VE16** results are indicated with solid lines, **GL15** results are shown with dashed lines, and computations based on the **Lovell et al. (2016)** implementation with dotted lines; in the latter case we show the individual data points with empty squares. In the right hand panel we show **CLASS** results with thin lines and **CAMB** results with thick lines; we also show fits to the **VE16 (GL15)** results with green (orange) lines. We indicate the fitting parameters for equation 3 in the figure legend.

Part of the challenge in setting limits through these studies is the difficulty in selecting a lower effective prior on the parameters. m_{th} of viable true thermal relic models is $\gtrsim 100$ MeV (Depta et al. 2019; Sabti et al. 2020) and is CDM, whereas the effective m_{th} for a classical axion model may well be much larger than this, and all at much larger values than the 1-10 keV expected for WDM. One approach is to instead constraint $1/m_{\text{th}}$, which for CDM = 0 keV^{-1} . This option evades the infinity but still creates a problem in logarithmic limits, a problem that is shared by M_{hm} . Most studies typically quote a limit on each parameter at 95 per cent confidence level (95 C. L.), based on the probability distribution of a posterior likelihood. Some studies also quote the highest M_{hm} (lowest m_{th}) for which the likelihood is 5 per cent of the maximum likelihood amplitude (5 M. L.). The latter measure is more conservative and evades the issue of how to determine the lower end of the prior. Therefore, we will set a preference to use this option in what follows, including inferring this result from paper results where possible.

Early Universe constraints. If N_2 and N_3 are sufficiently long lived, with lifetime $\tau > 0.1$ sec, they will inhibit baryogenesis, it is thus possible to show that $L_6 < 2500$ (Serpico & Raffelt 2005). Moreover, it is conceivable that if a sufficient fraction of the sterile neutrinos remain relativistic to late times, they may add a contribution to the number of relativistic degrees of freedom, N_{eff} . Our **CLASS** calculations return $\Delta N_{\text{eff}} < 1.1 \times 10^{-3}$ for all **VE16** and **GL15** models, which is significantly smaller than the ~ 0.35 figure (95 C. L.) of Planck Collaboration et al. (2020). We present these results in more detail in appendix A.

The Lyman- α forest. Lyman- α constraints take advantage of the suppression of structure at redshifts $4 < z < 6$. They examine fine hydrogen absorption features in the spectra of high redshift quasars – the Lyman- α forest – to infer the amount of structure present in the gas, and convolve these results with expectations for the properties of gas physics to obtain the underlying dark matter distribution. Progressively stronger constraints have been reported, from $m_{\text{th}} > 3.3$ keV (Viel et al. 2005) at 95 C. L. through to $m_{\text{th}} > 5.2$ keV (95 C. L.) (Iršič et al. 2017) (see also Murgia et al. 2017); we infer

$m_{\text{th}} > 4.7$ keV 5 M. L. for these data. Arguably the primary source of uncertainty is the thermal history, which may either mimic or obscure a dark matter power spectrum cutoff (Garzilli et al. 2017). A recent analysis by Villasenor et al. (2022) used new data sets and a different approach to the thermal history. They set a limit of > 3.1 keV (95 C. L.; we infer > 3.0 keV for 5 M. L.) and reported a weak preference for $m_{\text{th}} = 4.5^{+50}_{-1.4}$ keV over the CDM model.

Gravitation lensing. While the Lyman α forest studies use a background light source to detect a power spectrum cutoff through absorption, gravitational lensing experiments instead infer dark matter properties from how the background source is either distorted or magnified. The background light is lensed by a foreground dark matter halo – typically an isolated elliptical galaxy – and the degree of dark matter substructure is determined by the degree to which the lensing signal deviates from that expected for a smooth lens. This method has the potential to detect dark matter haloes down to $10^6 M_{\odot}$, where haloes are expected to contain no gas and thus remain dark. The two subbranches of lensing relevant for linear matter power spectrum studies are flux anomalies, in which the background source is a multiply imaged quasar, and gravitational imaging, which instead analyses lensed images of extended galaxies.

The gravitational lensing method has successfully detected several massive ($> 10^9 M_{\odot}$) haloes (Vegetti et al. 2010; Hezaveh et al. 2016), but not to a degree sufficient to compute strong constraints on the WDM model (Vegetti et al. 2018; Ritondale et al. 2019), and Euclid and the Vera C. Rubin Observatory (VCRO) will not have enough angular resolution to improve the constraints (O’Riordan et al. 2023). It is expected that high resolution imaging from the *European Extremely Large Telescope (E-ELT)* or very large baseline interferometry (VLBI) coupled to the square kilometre-array (SKA McKean et al. 2015; Powell et al. 2023) will be required to obtain sufficient statistics. Recent work in the flux anomalies side has claimed stronger constraints: Gilman et al. (2019) reports $m_{\text{th}} > 5.2$ keV 95 C. L. (> 3.2 keV at 5 M. L.), and Hsueh et al.

(2019) find $m_{\text{th}} > 5.58$ keV 95 C. L.², although the latter also reports the role of systematic uncertainties that require further study to refine this constraint. The *Euclid* mission may detect enough flux anomalies systems to discern whether the flux anomaly distribution is better described by CDM or WDM (Harvey et al. 2020).

Stellar stream gaps. An alternative method for detecting dark subhaloes is to search for their impact on gaps in stellar streams up to 40 kpc from the MW centre. Stellar streams are generated through the tidal stripping of globular clusters and satellite galaxies by the MW, and are expected to be very smooth in their light profile. The detection of kinks or gaps in a stream is then evidence for a past interaction with a perturber, including dark matter subhaloes. One reported detection of such a perturbation was made by Bonaca et al. (2019) (see also Ibata et al. 2020). Banik et al. (2021) reported $m_{\text{th}} > 4.9$ keV (95 C. L.) based on expectations for the MW subhalo mass function in WDM. However, the subhalo mass function in the central < 40 kpc differs less from CDM than is the case for the halo as a whole (Lovell et al. 2021); taking this factor into account weakens the constraint to $m_{\text{th}} > 2.1$ keV (95 C. L.).

High redshift constraints. The previous three types of studies looked for gravitationally induced distortions on observables. One further approach is to detect light from dwarf galaxies, whose number density is suppressed in WDM models. One such source of light is low mass galaxies in the early Universe, the presence or absence of which impacts the rate of reionization and thus determines when the Universe becomes transparent to visible light/mildly opaque to CMB photons. Various studies have considered the possibility of detecting these galaxies directly or instead comparing to reionization constraints. This possibility has been considered using a variety of simulation- and semi-analytic model-based approaches (Bose et al. 2016b; Menci et al. 2016; Rudakovskiy & Iakubovskiy 2016; Lovell et al. 2019a; Rudakovskiy et al. 2021; Kurmus et al. 2022; Maio & Viel 2022). These papers reveal that the impact of the cutoff is highly degenerate with gas physics processes such as the escape fraction of photons, and are therefore results in constraints weaker than those of the other observables listed above. The reported limits include $m_{\text{th}} > 2.4$ keV (95 C. L., Menci et al. 2016), and $m_{\text{th}} > 2$ keV (Rudakovskiy & Iakubovskiy 2016; Maio & Viel 2022).

MW satellite counts The final method that we will consider here for generating constraints is the detection of MW satellite galaxies. The MW satellites are the faintest observable galaxies, and therefore probe the edge of reionization as well as the subhalo mass function at $\sim 10^9 M_{\odot}$. Constraints rely on estimating the true number of MW satellites: approximately 50 are known (e.g. Bechtol et al. 2015; Drlica-Wagner et al. 2015; Torrealba et al. 2016; Koposov et al. 2018) and the number of undetected satellites are inferred from completeness limits due to depth and sky coverage. Very conservative limits can be obtained for values of $m_{\text{th}} < 1.6$ keV where the number of satellites generated is even smaller than the number of known MW satellites (Lovell et al. 2014).

Stronger limits require an understanding of the sky coverage selection function discussed above as well as physical processes such as the evacuation of gas from low mass haloes during reionization, the disruption of satellites by the MW disc, uncertainties in the MW halo mass, stochastic variations in halo assembly and the role of the Large Magellanic Cloud (LMC). Different assumptions in these areas can lead to dramatic differences in the number of predicted

satellites: the compilation by Kim et al. (2018) reports 120-150 satellites, the analysis by Newton et al. (2018) expects ~ 120 satellites, and Nadler et al. (2020) instead predicts of order 220. These results are key inputs for further studies of both WDM generally (Enzi et al. 2021; Nadler et al. 2021; Newton et al. 2021) and N_1 (Dekker et al. 2022; Zelko et al. 2022). In such studies, the satellite counts typically generate the strongest constraints of any observation: $M_{\text{hm}} < 8.5 \times 10^8 M_{\odot}$ (5 M. L.) for Enzi et al. (2021) and $M_{\text{hm}} < 2.5 \times 10^7 M_{\odot}$ (5 M. L.) for Nadler et al. (2021). As we will demonstrate below, the difference between these results brackets the allowed range for 3.55 keV line-compliant N_1 .

MW satellite structure. We end this review on the interplay between the WDM model and astrophysical observations with a discussion of the structure of MW satellites. The density of haloes with masses around the cutoff scale is suppressed in WDM relative to CDM (Colín et al. 2000; Lovell et al. 2012), and the degree of suppression is sufficient to explain a claimed discrepancy in the masses of subhaloes in CDM simulations versus observed satellites known as the ‘Too Big To Fail’ problem (Boylan-Kolchin et al. 2011, 2012; Lovell et al. 2012; Horiuchi et al. 2016; Lovell et al. 2017a,b; Bozek et al. 2019; Lovell & Zavala 2023). In principle, the density profiles of these satellites are the single most informative source for discriminating between different dark matter models: from high concentration cusps in CDM (Navarro et al. 1996b, 1997) to lower concentration cusps in WDM (Lovell et al. 2014); from self-interacting dark matter (SIDM) cores (Vogelsberger et al. 2012) to the very steep gravothermally collapsed cusps in extreme SIDM models (Zavala et al. 2019) and even the solitons of fuzzy dark matter (Nori et al. 2022). However, in the faintest systems it is very challenging to obtain enough stars to compute a density profile, and in brighter galaxies supernova feedback may play a confounding role (Navarro et al. 1996a; Pontzen & Governato 2012). Therefore, we do not attempt to provide WDM parameter constraints using satellite densities but highlight the importance of this observable for future dark matter studies.

4.3 Comparison to sterile neutrino parameter relations

In the previous two subsections we have presented limits from observations on N_1 /WDM parameters. X-ray non-detections enforce lower values of $\sin^2(2\theta)$, and WDM structure formation arguments decrease the allowed M_{hm} . Given that $\sin^2(2\theta)$ and M_{hm} are anti-correlated, it is therefore possible to compare these in tension to estimate the optimal N_1 parameters, if any, that are permitted by the observations or even preferred by reported detections.

In Fig. 6, we compare some of the X-ray and structure formation constraints listed above to the equation 3 fits to VE16 and GL15. We choose the CAMB calculations as these return more conservative M_{hm} values. Upper limits on M_{hm} are shown as horizontal lines with down-facing arrows, and upper limits on $\sin^2(2\theta)$ from X-ray studies are shown vertical lines with left-facing arrows; X-ray detections are shown as 1σ error bars. Each constraint only applies to either M_{hm} or $\sin^2(2\theta)$, and therefore its line applies across all of the presented parameter space; we draw short lines for the sake of clarity. We include four reported detections that span a range of targets: the M31 detection of Boyarsky et al. (2014), the galaxy cluster stack of Bulbul et al. (2014), the Galactic Bulge detection by Hofmann & Wegg (2019), and the outer MW halo detection of Cappelluti et al. (2018) when adopting the high-mass MW halo parameters. We represent non-detections with two of the most stringent available: the galaxy stack of Anderson et al. (2015) and the MW halo work of Sicilian et al. (2022) (for further analysis of the MW halo

² We do not infer a 5 M. L. limit for this result because the joint posterior amplitude is higher than 5 per cent of its maximum at all quoted masses.

see Dessert et al. 2020b; Boyarsky et al. 2020; Dessert et al. 2020a). Finally, for M_{hm} constraints we include five studies that quote, or from which we can obtain, 5 M. L. limits: two Lyman- α results (Iršič et al. 2017; Villaseñor et al. 2022), one gravitational lensing study (Gilman et al. 2020) and two combined-observation analyses that are in practice dominated by MW satellite counts (Enzi et al. 2021; Nadler et al. 2021)³.

In both the X-ray observations and the structure formation analyses, there is a wide variety of inconsistent constraints, some of which are in strong tension with both N_1 model predictions. The satellite counts in Nadler et al. (2021) are incompatible with any part of the suggested N_1 parameter space, with $M_{\text{hm}} < 5 \times 10^7 M_\odot$ whereas the alternative analysis by Enzi et al. (2021) is consistent with all models but for the VE16 model with $\sin^2(2\theta) < 7 \times 10^{-11}$. These studies are strongly dependent on the modelling of the LMC satellite contribution, the disruption of satellites by the disc, and the mass of MW halo, each of which leads to the differences in these results. There is similar disagreement within the Lyman- α bounds, where the Iršič et al. (2017) limit rules out all N_1 models while Villaseñor et al. (2022) is consistent with GL15 for $\sin^2(2\theta) > 3 \times 10^{-11}$. The Gilman et al. (2020) limit is consistent with GL15 for $\sin^2(2\theta) > 4 \times 10^{-11}$ and rules out all of the VE16 options.

The X-ray results are similarly inconsistent. We quote two non-detection studies, Sicilian et al. (2022) and Anderson et al. (2015), that are strongly constraining. The Sicilian et al. (2022) result permits $\sin^2(2\theta) < 2 \times 10^{-11}$, which is consistent with the Hofmann & Wegg (2019) detection but in some tension with the other. It would also require $M_{\text{hm}} > 7 \times 10^8 M_\odot$ for GL15. The Anderson et al. (2015) analysis is instead inconsistent with all of the allowed N_1 range. As for the reported detections, there is no one value of $\sin^2(2\theta)$ that is consistent with the 1σ ranges of all four. Adopting the value of 5×10^{-11} would represent a median between the four observations; if one instead posited that there is an undetected systematic uncertainty in the MW halo-derived results – both for the Hofmann & Wegg (2019) detection and for the limits by Dessert et al. (2020b,a); Sicilian et al. (2022) – that underestimates $\sin^2(2\theta)$ then one can make a case for 6×10^{-11} .

The question then becomes how to process these data into a coherent picture. The simplest approach is to take the most stringent constraints at face value, in which case both of the N_1 implementations discussed here are ruled out through a combination of the Anderson et al. (2015) galaxy stack and the Nadler et al. (2021) satellite counts. One then has to consider either that further iterations of the N_1 momentum distribution calculation will return values of M_{hm} that are lower by at least a factor of 20 compared to GL15, in order to obtain $M_{\text{hm}} < 5 \times 10^7 M_\odot$ at $\sin^2(2\theta) \sim 1 \times 10^{-11}$, or that resonantly produced $m_s = 7.1$ keV N_1 s as a whole are not viable and should be discarded as a dark matter candidate. If one were to be more optimistic, one could attempt to determine a provisional value of $\sin^2(2\theta)$, first by comparing the detections and then factoring in those X-ray and structure formation constraints that do result in a coherent $\sin^2(2\theta)$ – M_{hm} pair. The rough mid-point of the reported detections would return $\sin^2(2\theta) \sim 5 \times 10^{-11}$; relaxing the contribution of the MW halo could instead lead to 6×10^{-11} and then $M_{\text{hm}} \sim 3.0 \times 10^8 M_\odot$ using GL15. This choice still gives $\sin^2(2\theta)$ 3 \times the Sicilian et al. (2022) constraint and M_{hm} 3 \times higher

than the Iršič et al. (2017) constraint. Given that privileging one constraint will lead to greater tension with the other, we will argue that the single best value of $\sin^2(2\theta)$ for future study is $\sin^2(2\theta) = 6 \times 10^{-11}$, with $M_{\text{hm}} \sim 3.0 \times 10^8 M_\odot$ – and by extension $m_{\text{th}} \sim 3.5$ keV – as calculated with GL15. This value is also well within the preferred region for m_{th} determined by Villaseñor et al. (2022). We focus on this model for future study and for a comprehensive evaluation together with the strongest reported constraints.

5 CONCLUSIONS

The resonantly produced sterile neutrino (N_1) constitutes a compelling dark matter candidate for several reasons. It is part of a larger theory that may also explain neutrino oscillations and baryogenesis (Dodelson & Widrow 1994; Dolgov & Hansen 2002; Asaka & Shaposhnikov 2005; Laine & Shaposhnikov 2008; Boyarsky et al. 2009a), as well as adding right-handed neutrinos to the standard model. It is also accessible to astronomical experiments, through its decay into X-rays for large mixing angles (Pal & Wolfenstein 1982) and its erasure of structure at small mixing angles (Dodelson & Widrow 1994; Shi & Fuller 1999; Laine & Shaposhnikov 2008; Lovell et al. 2016). Detections of an X-ray signal claimed to be compatible with the decay of a N_1 with mass $m_s = 7.1$ keV and mixing angle $\sin^2(2\theta) = [2, 20] \times 10^{-11}$ add extra motivation. In this paper we revisit the physics behind N_1 production and its role in neutrino oscillations and baryons, present how different computational methods reach different conclusions for the linear matter power spectrum, and compare the results to observational constraints.

The neutrino minimal standard model (ν MSM) proposes the addition of three sterile neutrinos to the standard model. If two of these sterile neutrinos have masses at the GeV scale (N_2 and N_3) and N_1 is at the keV scale, N_2 and N_3 can facilitate baryogenesis and neutrino oscillations while N_1 is a dark matter candidate. The same process that leads N_2 and N_3 to generate the baryon asymmetry of the Universe may also lead to a lepton asymmetry at later times, which then enables the resonant production of N_1 . This resonant production leads to a momentum distribution that is skewed towards lower momenta than is the case for non-resonant production. The result is that the model behaves as WDM.

Two different publicly available codes – published in VE16 and GL15 – compute the momentum distributions for N_1 , determining the correct value of the lepton asymmetry, L_6 , to obtain the required dark matter abundance. We echo the result of VE16 in demonstrating that their code generates a warmer matter power spectrum than does GL15 (Fig. 2), and also find that the choice of Boltzmann solver is non-trivial (Fig. 3). Sterile neutrino models are often approximated by thermal relic power spectra: we show that the thermal relic model overestimates the power in CLASS-computed spectra for wavenumbers $k < k_{\text{hm}}$ by < 10 per cent for all of the $\sin^2(2\theta)$ values considered, whereas this model overestimates the GL15 power in the same range by up to 20 per cent, especially for larger $\sin^2(2\theta)$ (Fig. 4). The value of L_6 for VE16 and the chosen implementation of GL15 varies by 26 per cent (Fig. 5), but further implementations will differ by a factor of 10 (GL15). We also compute the half-mode mass M_{hm} as a function of $\sin^2(2\theta)$, and show this variable can vary by up to $2 \times 10^8 M_\odot$ between the two implementations.

We discuss the current status of constraints of dark matter decay from X-rays and the limits on the WDM cutoff scale from structure formation measurements. We present four detections of the 3.55 keV line centred on $\sin^2(2\theta) \sim 5 \times 10^{-11}$ and several non-detections that

³ Strong constraints have also been presented by Kim et al. (2018) ($m_{\text{th}} > 4$ keV, MW satellite counts) and Hsueh et al. (2019) ($m_{\text{th}} > 5.3, 95$ C. L., gravitational lensing); it is not possible to obtain 5 M. L. limits from these studies.

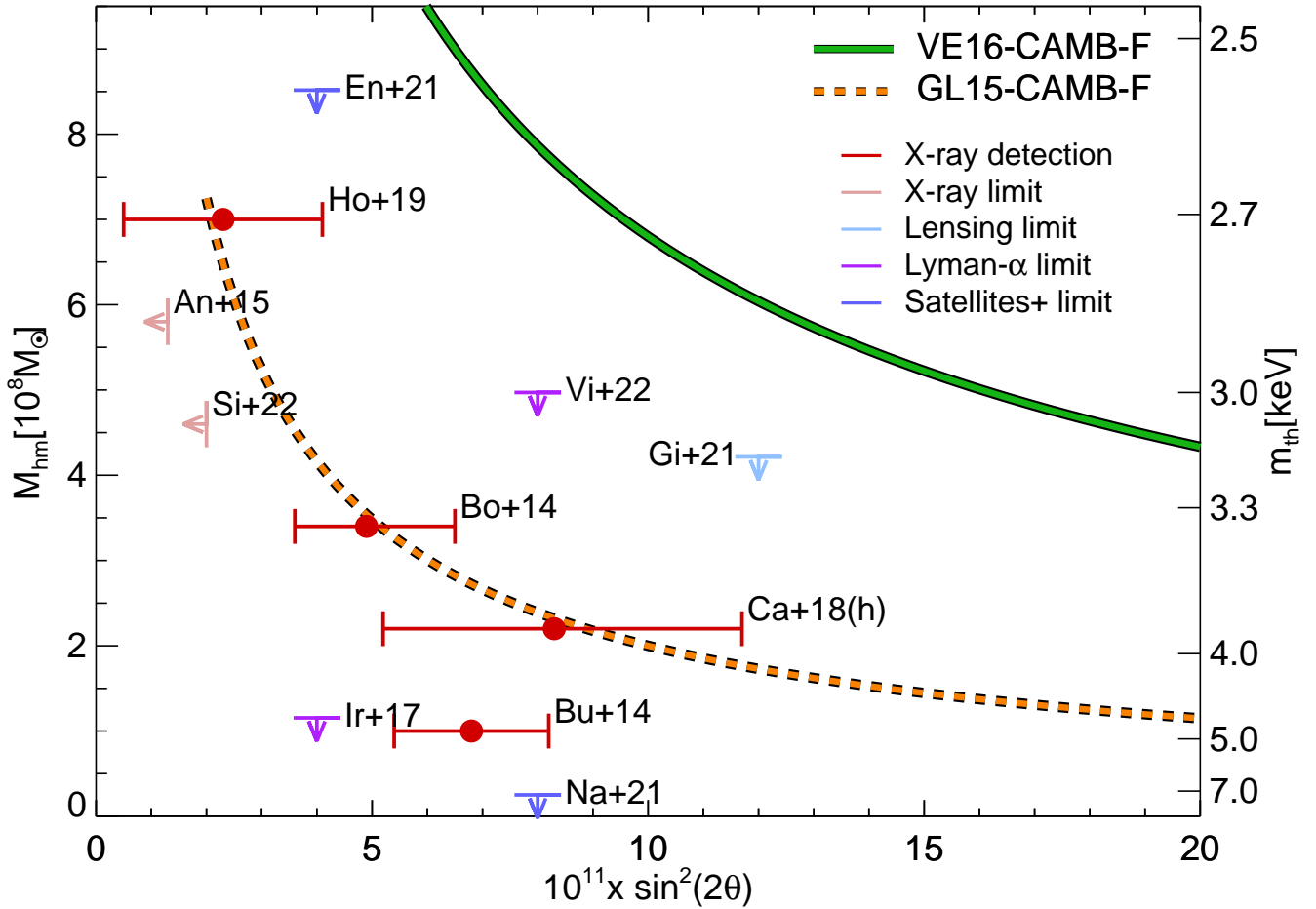


Figure 6. Constraints on the half-mode mass M_{hm} as a function of mixing angle with the corresponding thermal relic particle mass m_{th} indicated on the right-hand y-axis. The fits to **VE16** and **GL15** from Fig. 5 – both using **CAMB** – are reproduced as solid green and dashed orange lines respectively. Reported 3.55 keV line detections are indicated as red error bars and reflect 1σ uncertainties. X-ray non-detection-derived upper limits on the mixing angle are indicated with pink vertical lines, and upper limits on M_{hm} are shown with horizontal lines; the colours correspond to different types of observations as indicated in the figure legend. The x -axis location of M_{hm} constraints is arbitrary, as is the y -axis location of the X-ray constraints and detections.

prefer $\sin^2(2\theta) < 2 \times 10^{-11}$. We also discuss structure formation constraints on M_{hm} from the Lyman- α forest, gravitational lensing, stream gaps, and MW satellite counts. We show that the satellite counts currently offer the strongest constraints, and competing analyses offer limits that bracket the N_1 M_{hm} range: $M_{\text{hm}} < 8.5 \times 10^8 M_{\odot}$ at 5 M. L. for [Enzi et al. \(2021\)](#) and $M_{\text{hm}} < 3 \times 10^7 M_{\odot}$ at 5 M. L. for [Nadler et al. \(2021\)](#) (Fig. 6). If we adopt the most stringent published constraints, then N_1 dark matter is ruled out; if we instead take an optimistic approach then the combination of $\sin^2(2\theta)$ and M_{hm} constraints suggests the average detection $\sin^2(2\theta)$ of $\sim 6 \times 10^{-11}$ is most likely.

The clearest test of this result in the near future is the launch of the *XRISM* mission. This facility features a high resolution calorimeter that will measure the widths of X-ray lines, which in clusters of galaxies are characteristically larger for dark matter decay ($500 - 700 \text{ km s}^{-1}$) than for astrophysical lines ($< 200 \text{ km s}^{-1}$). The performance verification (PV) phase for *XRISM* will include the following guaranteed observation time: 280 ks for the Perseus cluster – comparable to the 230 ks obtained by *Hitomi* before that mission was lost – plus 500 ks of the Virgo cluster, 150 ks of the Centaurus cluster and 200 ks of the Coma cluster, with an addi-

tional 200 ks for Perseus and 100 ks for Coma if conditions allow (<https://heasarc.gsfc.nasa.gov/docs/xrism/timelines/pvtargets.html>).

The Perseus, Virgo, and Centaurus decay line parameters were estimated for the *XRISM* field-of-view in [Lovell et al. \(2019b\)](#), with on-centre line-of-sight velocity dispersions $\sigma_{\text{1D}} \approx \sim 600, \sim 470$ and $\sim 450 \text{ km s}^{-1}$ respectively. The Coma cluster mass and distance parameters are approximately the same as Perseus and therefore this cluster should also have $\sigma_{\text{1D}} \sim 600 \text{ km s}^{-1}$. [Lovell et al. \(2019b\)](#) also estimated that the expected flux from Virgo should be twice that of Perseus, thus when combined with the PV time allocations suggests that Virgo may present the first opportunity to detect the line, prior to the consideration of other observational effects. [Bulbul et al. \(2014\)](#) estimated that a Perseus line of $\sigma_{\text{1D}} = 1300 \text{ km s}^{-1}$ – the velocity dispersion of the Perseus member galaxies rather than the dark matter – could be detected with 1 Msec of exposure, which is $> 2\times$ the maximum Perseus PV allocation but to first order returns the same number of photons as the 500 ks Virgo allocation, given that the expected Virgo flux is twice that of Perseus and also that the line width in Virgo is half that of the [Bulbul et al. \(2014\)](#)-Perseus estimate. The tentative detection of a line in Virgo would then motivate dedicated, post-PV campaigns to measure the line width in other nearby clusters

and ascertain whether or not its properties strictly adhere to the dark matter content.

In the event that such a detection is made, two questions will arise: (i) whether the line is indeed dark matter decay, and (ii) whether this candidate is N_1 dark matter. First, the following steps will need to be taken to ascertain that the line is dark matter decay:

- Obtain careful estimates of the astrophysical background signal in galaxies and galaxy clusters, empirically from observations and also from mock observations of simulations.
- Perform observations of targets where the amount of hot gas is minimized, such as the Bullet cluster (Boyarsky et al. 2008) and the Draco dSph (Lovell et al. 2015).
- Develop sophisticated models of the MW halo mass distribution, including adiabatic contraction, to compare to blank sky X-ray observations.

Second, we set out the issues to be addressed in ascertaining whether this decaying dark matter is N_1 rather than a still more exotic candidate:

- Refine the computations of early Universe physics to ascertain as accurately as possible the initial lepton asymmetry and the momentum distribution.
- Identify whether differences between the full N_1 matter power spectra calculations and the thermal relic approximation are significant for structure formation constraints.
- Ascertain the source of the current incompatibility in MW satellite counts, and then resolve the discrepancy, including through new observations by the upcoming *VCRO-LSST* facility (Ivezic et al. 2019).
- Perform high resolution gravitational imaging studies with the E-ELT to measure the $\sim 10^8 M_\odot$ halo mass function (Vegetti et al. 2018).
- Continue to develop models of galaxy formation that accurately follow processes as diverse as star formation, supernova feedback, magnetic fields, and stripping by host galaxies in order to predict halo density profiles and luminosity fractions, particularly in dSph (Gutcke et al. 2022).

One final consideration is the contribution from particle physics experiments. Generating measurable amount of N_1 in an experiment is a formidable challenge, where even the anticipated upgrades to the KATRIN experiment are limited to probing $\sin^2(2\theta) > 10^{-9}$ (Aker et al. 2022), some two orders of magnitude higher than the lowest 3.55 keV line-compatible models. Other experiments are instead searching for N_2 and N_3 . The DUNE experiment will probe neutrino physics to ascertain the neutrino mass hierarchy and measure the charge-parity-violating phase, and has some potential to constrain the parameter space of N_2 and N_3 (DUNE Collaboration et al. 2015, 2020); it will come online in the second half of this decade. Two proposed CERN experiments, SHiP (Ahdida et al. 2019) and MATH-USLA (Curtin et al. 2019), would probe rare events in which N_2 and N_3 are produced and then decay into products that are subsequently detected. The combination of experiment, X-ray observations, and structure formation constraints will then have played a key role in identifying whether N_1 is indeed the dark matter.

ACKNOWLEDGEMENTS

MRL would like to thank Jesús Zavala, Tamar Meshveliani, Esra Bulbul, Michael Boylan-Kolchin, Francis-Yan Cyr-Racine and Simona Vegetti for useful comments.

DATA AVAILABILITY

The original codes for VE16 and GL15 are available at <https://github.com/ntveem/sterile-dm> and <http://www.laine.itp.unibe.ch/dmphenol/> respectively.

REFERENCES

- Abratenko P., et al., 2023, *Phys. Rev. Lett.*, **130**, 011801
- Agafonova N., et al., 2022, *arXiv e-prints*, p. arXiv:2211.04636
- Aharonian F. A., et al., 2017, *ApJ*, **837**, L15
- Ahdida C., et al., 2019, *Journal of High Energy Physics*, **2019**, 77
- Aker M., et al., 2022, *Journal of Physics G Nuclear Physics*, **49**, 100501
- An R., Gluscevic V., Calabrese E., Hill J. C., 2022, *J. Cosmology Astropart. Phys.*, **2022**, 002
- An R., Gluscevic V., Nadler E. O., Zhang Y., 2023, *arXiv e-prints*, p. arXiv:2301.08299
- Anderson M. E., Churazov E., Bregman J. N., 2015, *MNRAS*, **452**, 3905
- Asaka T., Shaposhnikov M., 2005, *Physics Letters B*, **620**, 17
- Athanassopoulos C., et al., 1996, *Phys. Rev. Lett.*, **77**, 3082
- Banik N., Bovy J., Bertone G., Erkal D., de Boer T. J. L., 2021, *J. Cosmology Astropart. Phys.*, **2021**, 043
- Bardeen J. M., Bond J. R., Kaiser N., Szalay A. S., 1986, *ApJ*, **304**, 15
- Barger V., Phillips R. J. N., Sarkar S., 1995, *Physics Letters B*, **352**, 365
- Bechtol K., et al., 2015, *ApJ*, **807**, 50
- Bode P., Ostriker J. P., Turok N., 2001, *ApJ*, **556**, 93
- Bonaca A., Hogg D. W., Price-Whelan A. M., Conroy C., 2019, *ApJ*, **880**, 38
- Bond J. R., Szalay A. S., 1983, *ApJ*, **274**, 443
- Bose S., Hellwing W. A., Frenk C. S., Jenkins A., Lovell M. R., Helly J. C., Li B., 2016a, *MNRAS*, **455**, 318
- Bose S., Frenk C. S., Hou J., Lacey C. G., Lovell M. R., 2016b, *MNRAS*, **463**, 3848
- Boyarsky A., Ruchayskiy O., Markevitch M., 2008, *ApJ*, **673**, 752
- Boyarsky A., Ruchayskiy O., Shaposhnikov M., 2009a, *Annual Review of Nuclear and Particle Science*, **59**, 191
- Boyarsky A., Lesgourgues J., Ruchayskiy O., Viel M., 2009b, *Physical Review Letters*, **102**, 201304
- Boyarsky A., Ruchayskiy O., Iakubovskiy D., Franse J., 2014, *Physical Review Letters*, **113**, 251301
- Boyarsky A., Malyshev D., Ruchayskiy O., Savchenko D., 2020, *arXiv e-prints*, p. arXiv:2004.06601
- Boylan-Kolchin M., Bullock J. S., Kaplinghat M., 2011, *MNRAS*, **415**, L40
- Boylan-Kolchin M., Bullock J. S., Kaplinghat M., 2012, *MNRAS*, **422**, 1203
- Bozek B., et al., 2019, *MNRAS*, **483**, 4086
- Bulbul E., Markevitch M., Foster A., Smith R. K., Loewenstein M., Randall S. W., 2014, *ApJ*, **789**, 13
- Cappelluti N., et al., 2018, *ApJ*, **854**, 179
- Colín P., Avila-Reese V., Valenzuela O., 2000, *ApJ*, **542**, 622
- Conlon J. P., Powell A. J., 2015, *J. Cosmology Astropart. Phys.*, **2015**, 019
- Curtin D., et al., 2019, *Reports on Progress in Physics*, **82**, 116201
- DUNE Collaboration et al., 2015, *arXiv e-prints*, p. arXiv:1512.06148
- DUNE Collaboration et al., 2020, *arXiv e-prints*, p. arXiv:2008.12769
- Dekker A., Ando S., Correa C. A., Ng K. C. Y., 2022, *Phys. Rev. D*, **106**, 123026
- Depta P. F., Hufnagel M., Schmidt-Hoberg K., Wild S., 2019, *J. Cosmology Astropart. Phys.*, **2019**, 029
- Dessert C., Rodd N. L., Safdi B. R., 2020a, *Physics of the Dark Universe*, **30**, 100656
- Dessert C., Rodd N. L., Safdi B. R., 2020b, *Science*, **367**, 1465
- Dodelson S., Widrow L. M., 1994, *Physical Review Letters*, **72**, 17
- Dolgov A., Hansen S., 2002, *Astropart. Phys.*, **16**, 339
- Drlica-Wagner A., et al., 2015, *ApJ*, **813**, 109
- Enzi W., et al., 2021, *MNRAS*, **506**, 5848
- Garzilli A., Boyarsky A., Ruchayskiy O., 2017, *Physics Letters B*, **773**, 258
- Gaskins J. M., 2016, *Contemporary Physics*, **57**, 496
- Ghiglieri J., Laine M., 2015, *Journal of High Energy Physics*, **2015**, 171

- Gilman D., Du X., Benson A., Birrer S., Nierenberg A., Treu T., 2019, *MNRAS*, p. L167
- Gilman D., Birrer S., Nierenberg A., Treu T., Du X., Benson A., 2020, *MNRAS*, 491, 6077
- Gu L., Kaastra J., Raassen A. J. J., Mullen P. D., Cumbee R. S., Lyons D., Stancil P. C., 2015, *A&A*, 584, L11
- Gutcke T. A., Pfrommer C., Bryan G. L., Pakmor R., Springel V., Naab T., 2022, *ApJ*, 941, 120
- Harvey D., Valkenburg W., Tamone A., Boyarsky A., Courbin F., Lovell M., 2020, *MNRAS*, 491, 4247
- Hezaveh Y. D., et al., 2016, *ApJ*, 823, 37
- Hofmann F., Wegg C., 2019, *A&A*, 625, L7
- Horiuchi S., Bozek B., Abazajian K. N., Boylan-Kolchin M., Bullock J. S., Garrison-Kimmel S., Onorbe J., 2016, *MNRAS*, 456, 4346
- Hsueh J. W., Enzi W., Vegetti S., Auger M. W., Fassnacht C. D., Despali G., Koopmans L. V. E., McKean J. P., 2019, *MNRAS*, p. 2780
- Humbert P., Lindner M., Smirnov J., 2015, *Journal of High Energy Physics*, 2015, 35
- Ibata R., Thomas G., Famaey B., Malhan K., Martin N., Monari G., 2020, *ApJ*, 891, 161
- Iršič V., et al., 2017, *Phys. Rev. D*, 96, 023522
- Ivezić Ž., et al., 2019, *ApJ*, 873, 111
- Jeltema T., Profumo S., 2015, *MNRAS*, 450, 2143
- Jeltema T., Profumo S., 2016, *MNRAS*, 458, 3592
- Kim S. Y., Peter A. H. G., Hargis J. R., 2018, *Phys. Rev. Lett.*, 121, 211302
- Koposov S. E., et al., 2018, *MNRAS*, 479, 5343
- Kurmus A., Bose S., Lovell M., Cyr-Racine F.-Y., Vogelsberger M., Pfrommer C., Zavala J., 2022, *MNRAS*, 516, 1524
- Laine M., Shaposhnikov M., 2008, *J. Cosmology Astropart. Phys.*, 6, 31
- Lesgourgues J., Tram T., 2011, *J. Cosmology Astropart. Phys.*, 2011, 032
- Lewis A., Challinor A., Lasenby A., 2000, *ApJ*, 538, 473
- Lovell M. R., Zavala J., 2023, *MNRAS*, 520, 1567
- Lovell M. R., et al., 2012, *MNRAS*, 420, 2318
- Lovell M. R., Frenk C. S., Eke V. R., Jenkins A., Gao L., Theuns T., 2014, *MNRAS*, 439, 300
- Lovell M. R., Bertone G., Boyarsky A., Jenkins A., Ruchayskiy O., 2015, *MNRAS*, 451, 1573
- Lovell M. R., et al., 2016, *MNRAS*, 461, 60
- Lovell M. R., Gonzalez-Perez V., Bose S., Boyarsky A., Cole S., Frenk C. S., Ruchayskiy O., 2017a, *MNRAS*, 468, 2836
- Lovell M. R., et al., 2017b, *MNRAS*, 468, 4285
- Lovell M. R., Zavala J., Vogelsberger M., 2019a, *MNRAS*, 485, 5474
- Lovell M. R., Iakubovskiy D., Barnes D., Bose S., Frenk C. S., Theuns T., Hellwing W. A., 2019b, *ApJ*, 875, L24
- Lovell M. R., Cautun M., Frenk C. S., Hellwing W. A., Newton O., 2021, *MNRAS*, 507, 4826
- Maio U., Viel M., 2022, arXiv e-prints, p. arXiv:2211.03620
- McKean J., et al., 2015, in *Advancing Astrophysics with the Square Kilometre Array (AASKA14)*. p. 84 (arXiv:1502.03362), doi:10.22323/1.215.0084
- Menci N., Grazian A., Castellano M., Sanchez N. G., 2016, *ApJ*, 825, L1
- Mention G., Fechner M., Lasserre T., Mueller T. A., Lhuillier D., Cribier M., Letourneau A., 2011, *Phys. Rev. D*, 83, 073006
- Merle A., Schneider A., Totzauer M., 2016, *J. Cosmology Astropart. Phys.*, 2016, 003
- Mikheev S. P., Smirnov A. I., 1986, *Nuovo Cimento C Geophysics Space Physics C*, 9, 17
- Murgia R., Merle A., Viel M., Totzauer M., Schneider A., 2017, *J. Cosmology Astropart. Phys.*, 2017, 046
- Nadler E. O., et al., 2020, *ApJ*, 893, 48
- Nadler E. O., Birrer S., Gilman D., Wechsler R. H., Du X., Benson A., Nierenberg A. M., Treu T., 2021, *ApJ*, 917, 7
- Navarro J. F., Eke V. R., Frenk C. S., 1996a, *MNRAS*, 283, L72
- Navarro J. F., Frenk C. S., White S. D. M., 1996b, *ApJ*, 462, 563
- Navarro J. F., Frenk C. S., White S. D. M., 1997, *ApJ*, 490, 493
- Newton O., Cautun M., Jenkins A., Frenk C. S., Helly J. C., 2018, *MNRAS*, 479, 2853
- Newton O., et al., 2021, *J. Cosmology Astropart. Phys.*, 2021, 062
- Nori M., Macciò A. V., Baldi M., 2022, arXiv e-prints, p. arXiv:2210.08022
- O’Riordan C. M., Despali G., Vegetti S., Lovell M. R., Molinè Á., 2023, *MNRAS*, 521, 2342
- Pal P. B., Wolfenstein L., 1982, *Phys. Rev. D*, 25, 766
- Petreczky P., 2012, *Journal of Physics G Nuclear Physics*, 39, 093002
- Planck Collaboration et al., 2016, *A&A*, 594, A13
- Planck Collaboration et al., 2020, *A&A*, 641, A6
- Pontzen A., Governato F., 2012, *MNRAS*, 421, 3464
- Powell D. M., Vegetti S., McKean J. P., White S. D. M., Ferreira E. G. M., May S., Spingola C., 2023, arXiv e-prints, p. arXiv:2302.10941
- Ritondale E., Vegetti S., Despali G., Auger M. W., Koopmans L. V. E., McKean J. P., 2019, *MNRAS*, 485, 2179
- Ruchayskiy O., et al., 2016, *MNRAS*, 460, 1390
- Rudakovskiy A., Iakubovskiy D., 2016, *J. Cosmology Astropart. Phys.*, 6, 017
- Rudakovskiy A., Mesinger A., Savchenko D., Gillet N., 2021, *MNRAS*, 507, 3046
- Sabti N., Alvey J., Escudero M., Fairbairn M., Blas D., 2020, *J. Cosmology Astropart. Phys.*, 2020, 004
- Serpico P. D., Raffelt G. G., 2005, *Phys. Rev. D*, 71, 127301
- Shah C., Dobrodey S., Bernitt S., Steinbrügge R., Crespo López-Urrutia J. R., Gu L., Kaastra J., 2016, *ApJ*, 833, 52
- Shi X., Fuller G. M., 1999, *Physical Review Letters*, 82, 2832
- Sicilian D., Lopez D., Moscetti M., Bulbul E., Cappelluti N., 2022, *ApJ*, 941, 2
- Terada Y., et al., 2021, *Journal of Astronomical Telescopes, Instruments, and Systems*, 7, 037001
- Torrealba G., Koposov S. E., Belokurov V., Irwin M., 2016, *MNRAS*, 459, 2370
- Vegetti S., Koopmans L. V. E., Bolton A., Treu T., Gavazzi R., 2010, *MNRAS*, 408, 1969
- Vegetti S., Despali G., Lovell M. R., Enzi W., 2018, *MNRAS*, 481, 3661
- Venumadhav T., Cyr-Racine F.-Y., Abazajian K. N., Hirata C. M., 2016, *Phys. Rev. D*, 94, 043515
- Viel M., Lesgourgues J., Haehnelt M. G., Matarrese S., Riotto A., 2005, *Phys. Rev. D*, 71, 063534
- Villasenor B., Robertson B., Madau P., Schneider E., 2022, arXiv e-prints, p. arXiv:2209.14220
- Vogelsberger M., Zavala J., Loeb A., 2012, *MNRAS*, 423, 3740
- Wolfenstein L., 1978, *Phys.Rev.*, D17, 2369
- Zavala J., Lovell M. R., Vogelsberger M., Burger J. D., 2019, *Phys. Rev. D*, 100, 063007
- Zelko I. A., Treu T., Abazajian K. N., Gilman D., Benson A. J., Birrer S., Nierenberg A. M., Kusenko A., 2022, *Phys. Rev. Lett.*, 129, 191301

APPENDIX A: THE EFFECTIVE NUMBER OF RELATIVISTIC DEGREES OF FREEDOM

An interesting corollary of the late transition from relativistic to non-relativistic properties for N_1 is the impact on N_{eff} , and whether this value is high enough to be measurable with current or future cosmological observations. We therefore compute values of the excess degrees of freedom due to N_1 , labelled ΔN_{eff} for the **VE16** and **GL15** models as a function of $\sin^2(2\theta)$; we apply the `CLASS` code for this task. We present the results in Fig. A1.

The value of ΔN_{eff} is inversely correlated with $\sin^2(2\theta)$, in line with the initial N_1 temperature distribution and the subsequent matter power spectrum cutoff. The highest value of ΔN_{eff} for **VE16** is 1.1×10^{-3} , at $\sin^2(2\theta) = 2 \times 10^{-11}$ and smoothly drops to 6.8×10^{-4} at $\sin^2(2\theta) = 2 \times 10^{-10}$. The same relation shape occurs for **GL15**, albeit with a lower normalization such that the highest value is 8.1×10^{-4} . These results are lower than the uncertainty in N_{eff} derived in [Planck Collaboration et al. \(2020\)](#) and therefore it is unlikely than any experiment can probe this result in the near future.

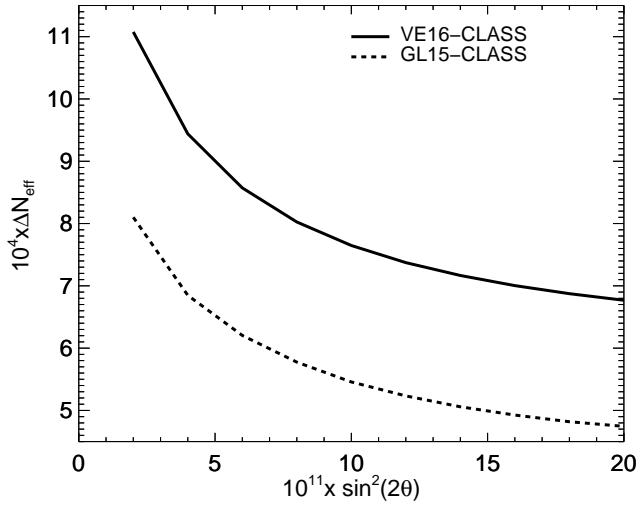


Figure A1. The relationship between $\sin^2(2\theta)$ and ΔN_{eff} for the two models when the `CLASS` code is applied to calculate the linear matter power spectrum. The [VE16](#) result is shown as a solid line and the [GL15](#) result is shown as a dashed line.

This paper has been typeset from a $\text{\TeX}/\text{\LaTeX}$ file prepared by the author.